ZIBELINE INTERNATIONAL™ PUBLISHING

ISSN: 2222-7059 (Print)
EISSN: 2222-7067 (Online)

Advances in Industrial Engineering and Management (AIEM)

DOI: http://doi.org/10.7508/aiem.01.2025.15.22

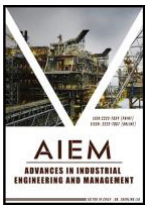

CrossMark

RESEARCH ARTICLE

AGING MECHANISM ANALYSIS IN NICKEL-COBALT-MANGANESE TERNARY BATTERIES BASED ON DRT TECHNOLOGY

Wenqing Wei, Yaomin Zhao*, Zenghui He, Qimeng Du, Xueling Wu, Siru Chen

School of Materials Electronics and Energy Storage, Zhongyuan University of Technology, Zhengzhou 450007, China
**Corresponding Author E-mail: zhaoyaomin0707@zut.edu.cn*

ARTICLE DETAILS

Article History:

Received 20 April 2025
Accepted 23 May 2025
Revised 5 June 2025
Available online 6 June 2025

ABSTRACT

This study investigates 18650-type $LiNi_{0.5}Co_{0.2}Mn_{0.3}O_2$ (NCM523)/graphite lithium-ion batteries, systematically collecting electrochemical impedance spectroscopy (EIS) data across various cycle numbers (CN20 to CN240) and SOC (3.0–4.2 V), and employs equivalent circuit models and distribution of relaxation times (DRT) techniques to reveal the multiscale dynamic behaviors and aging mechanisms within the battery. The results indicate that the ohmic resistance of the battery increases significantly with cycle number (2.6-fold from CN20 to CN240), independent of the state of charge, whereas the charge-transfer resistance is closely related to the state of charge but exhibits no significant overall aging trend, suggesting distinctly different aging mechanisms for the two. DRT analysis successfully deconvoluted five polarization processes: SEI/CEI film formation, positive/negative electrode charge transfer, and solid-phase diffusion, with polarization behavior dominated by diffusion control (P5). The impedance of positive/negative electrode charge transfer (P3/P4) and solid-phase diffusion (P5) is highly dependent on the state of charge, exhibiting variations in magnitude ranging from 10- to 740-fold within the same cycle, highlighting the heterogeneity of various dynamic processes. This study provides theoretical insights and data support for optimizing battery performance and extending battery lifespan.

KEYWORDS

Lithium-Ion Battery, Relaxation Time Distribution, Equivalent Circuit Simulation, Kinetic Process, Ageing Mechanism

1. INTRODUCTION

Lithium-ion batteries are widely used in portable electronic devices, pure electric vehicles, and energy storage systems due to their superior electrochemical performance, including high energy density, long service life, and low self-discharge rate (Sadeghi et al., 2023). Nickel-cobalt-manganese (NCM) materials are currently the most widely used cathode materials for lithium-ion batteries. During long-term cycling or high-rate operation, lithium-ion batteries undergo significant aging, resulting in capacity fade, impedance increase, and degradation of safety performance (Kebede, 2023). Moreover, factors such as different states of charge (SOC), temperature, and relaxation times significantly affect impedance. The lithium-ion battery system involves complex electrochemical processes, including lithium-ion diffusion in electrode materials and electrolytes, charge transfer (electrochemical reactions at the electrode-electrolyte interface), formation and evolution of the solid electrolyte interphase (SEI) film, and structural changes in electrode materials (Siroma and Kuratani, 2025). These processes play a critical role in battery cycling, but their identification is highly challenging. Elucidating the dynamic processes and aging mechanisms of lithium-ion batteries represents a significant challenge.

Electrochemical impedance spectroscopy (EIS), as a non-destructive testing method, reflects the internal dynamic characteristics of batteries through frequency-domain impedance data, serving as a critical tool for analyzing impedance, studying dynamics, and investigating aging mechanisms (Hu et al., 2023; Azizighalehsari et al., 2024). Many researchers utilize equivalent circuit models (ECM) to fit battery impedance spectra to extract parameters related to individual electrochemical processes occurring within the battery. For example, Ali Yousaf Kharal et al. employed a second-order RC equivalent circuit model and physics-based model fitting to EIS, thereby identifying material performance changes induced by cyclic aging (Kharal et al., 2025). Wenlin Zhang et al. employed a first-order RC equivalent circuit to analyze 36 different usage conditions of EIS, finding that, in addition

Quick Response Code	Access this article online	
	Website: www.aiem.com.my	DOI: 10.7508/aiem.01.2025.15.22

Cite The Article: Wei, W. Q., Zhao, Y. M., He, Z. H., Du, Q. M., Wu, X. L., Chen, S. R., (2025). Aging Mechanism Analysis in Nickel-Cobalt-Manganese Ternary Batteries based on Drt Technology. *Advances in Industrial Engineering and Management, 14(1): 15-22. Doi: 10.7508/aiem.01.2025.15.22*

to relaxation time, the historical usage patterns of the battery play a critical role in determining the battery impedance spectrum (Zhang et al., 2025). Analyzing EIS data is critical, but it often presents challenges due to the numerous possible equivalent circuits, requiring accurate analytical models. However, given the complexity of separating multiple electrochemical processes in EIS spectra, traditional equivalent circuit fitting, whether first-order or second-order, struggles to precisely resolve their contributions (Patel et al., 2025).

The distribution of relaxation times (DRT) method can effectively separate the aforementioned dynamic processes (Maradesa et al., 2024a). It has become a promising approach for EIS analysis. The DRT method transforms EIS data into a time-domain relaxation time spectrum, separating dynamic processes across different time scales, providing a high-resolution tool for studying the aging mechanisms of lithium-ion batteries (Plank et al., 2024; Iurilli et al., 2021; Jung et al., 2024). The core of the distribution of relaxation times technique lies in transforming frequency-domain impedance data into a time-domain relaxation time distribution, thereby revealing the dynamic variation characteristics of internal polarization impedance in batteries across different time scales (Maradesa et al., 2024b). Rong He et al. utilized the distribution of relaxation times to analyze the impedance of dynamic processes and corresponding time constants in three types of commercial batteries—$LiNi_{0.8}Co_{0.1}Mn_{0.1}O_2$, Li_xFePO_4, and $LiNi_xCo_yAl_zO_2$—at different aging stages, and through experimental measurements and multi-peak analysis of DRT, determined the impedance distribution characteristics of batteries with different materials during cycling (He et al., 2023). Muhammad Sohaib employed an n-order RC equivalent circuit based on Gaussian functions to achieve decoupling of overlapping electrochemical processes, thereby attributing four distinct electrochemical processes, based on their time constants, to four different DRT peaks corresponding to ohmic impedance, SEI film impedance, charge-transfer impedance, and diffusion impedance (Sohaib et al., 2025). Xing Zhou et al. combined distribution of relaxation times and physics-based modeling methods to analyze the electrochemical impedance spectra of NCM333/graphite lithium-ion batteries, classifying five types of dynamic processes based on their time constants: contact impedance, Li^+ transport through the SEI film, charge-transfer reaction, and diffusion impedance (Zhou et al., 2019). Pietro Iurilli et al. performed DRT analysis on the EIS spectra of commercial cylindrical lithium-ion batteries and laboratory-assembled coin half-cells, conducting a comparative analysis, and, combined with scanning electron microscopy testing, ultimately attributed the resolved peaks, based on their time constants, to six dynamic processes in the following order: electromagnetic effects, SEI film impedance, CEI film impedance, anode charge-transfer impedance, cathode charge-transfer impedance, and diffusion impedance (Iurilli et al., 2022). Tom Rüther et al. investigated the differences among individual battery cells, characterizing 92 single cells through impedance and other tests, and analyzed and validated the data using comprehensive DRT, attributing dynamic processes with different time constants to electromagnetic effects, charge transport at the passivation layer (SEI, CEI) and electrode interface, charge transfer and double-layer effects at the electrode interface, and solid-state diffusion within active material particles (Rüther et al., 2023). Yang Lu et al. analyzed the complex dynamic processes of different lithium-ion batteries based on time scales and performed decoupling identification, concluding that the dynamic processes of nickel-cobalt-manganese ternary batteries, based on their time constants, are sequentially attributed to SEI film impedance, CEI film impedance, anode charge-transfer impedance, cathode charge-transfer impedance, and diffusion impedance, comprising five components (Lu et al., 2022), which is largely consistent with the conclusions of Pietro Iurilli. However, numerous studies exhibit contradictions and inconsistencies.

This study systematically collected EIS data for 18650-type lithium-ion batteries with nickel-cobalt-manganese ternary material $LiNi_{0.5}Co_{0.2}Mn_{0.3}O_2$ (NCM523) as the cathode and graphite as the anode (hereafter abbreviated as Gra||NCM523) during the cyclic aging process at different life cycles and SOC (controlled by charge-discharge voltage methods). Utilizing DRT technology, a systematic quantitative analysis was conducted on various dynamic processes in the NCM lithium-ion battery system across different life cycles and SOC, and combined with the quantitative analysis results of equivalent circuit models, the dynamic processes and aging mechanisms in Gra||NCM523 lithium-ion batteries were elucidated.

2. Materials and Methods

2.1 Materials

The study utilized 18650-type NCM ternary lithium-ion batteries (Gra||NCM523, nominal capacity 2000 mAh) for data collection. The cyclic operation data (3.0 V to 4.2 V, 1C) were collected using an Arbin battery testing system (Arbin Instruments LBT 21084), with the testing

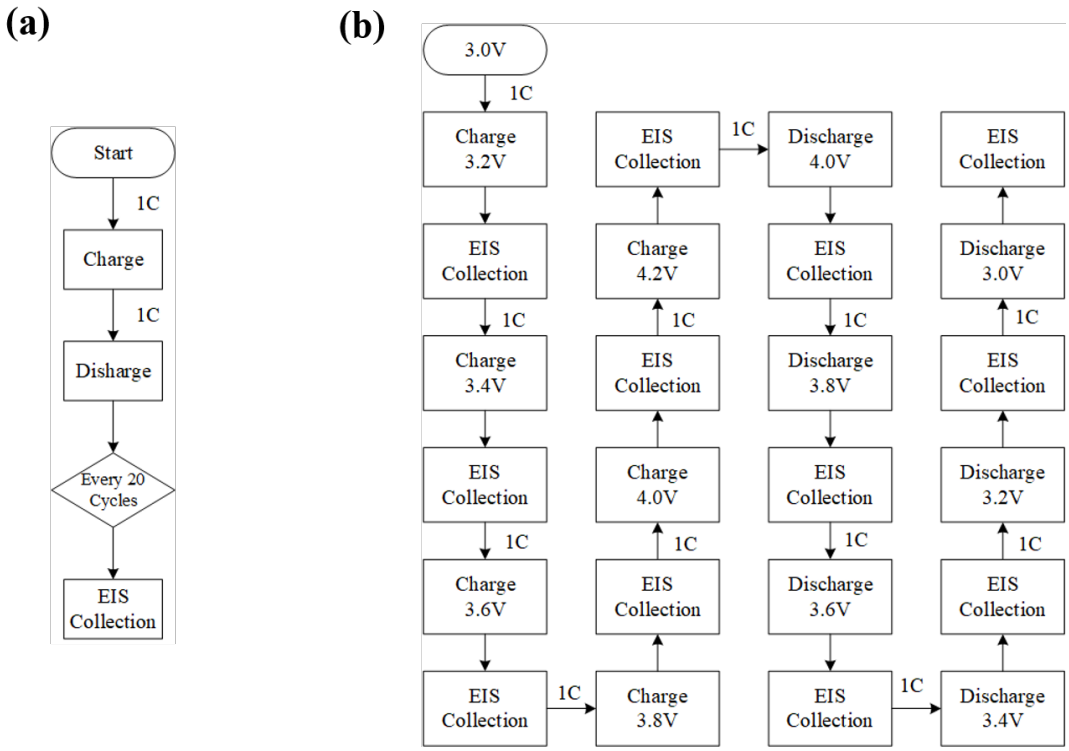

Figure 1: (a) Cyclic aging testing procedure; (b) EIS data collection procedure

procedure shown in Figure 1(a).Alternating current impedance tests of the battery at different charge-discharge voltages were performed using a Princeton VersaSTAT 3, with EIS data collected every 20 cycles at various charge-discharge voltages, following the collection procedure shown in Figure 1(b), with an amplitude of 10 mV and a frequency range of 10^{-5} to 10^{-2} Hz. The 20th cycle is abbreviated as CN20, the 40th cycle as CN40, and so forth. The testing environment temperature was consistently 25 °C.

2.2 First-Order RQ Equivalent Circuit Model

The typical EIS spectrum obtained is shown in Figure 2(a), consisting of an approximate semicircle in the mid-frequency region and a slanted line in the low-frequency region within the first quadrant. The high-frequency region corresponds to the battery's ohmic impedance R_{ohm}; the semicircle in the mid-frequency region corresponds to the battery's charge-transfer process, typically modeled by R_{ct} and CPEl in parallel, where R_{ct} represents the charge-transfer resistance of the electrode and CPE_l represents the constant phase element. The slanted line in the low-frequency region reflects the diffusion behavior of Li^+ between the electrode interface and the solution during the electrode reaction, represented by Warburg (W) impedance, namely the Li^+ diffusion impedance. This study exclusively employed the most commonly used first-order RQ equivalent circuit model for fitting, as shown in Figure 2(b). Here, R_o represents the ohmic impedance, R_{ct} represents the charge-transfer resistance of the electrode, CPE_l represents the constant phase element, and W_1 represents the Warburg impedance.

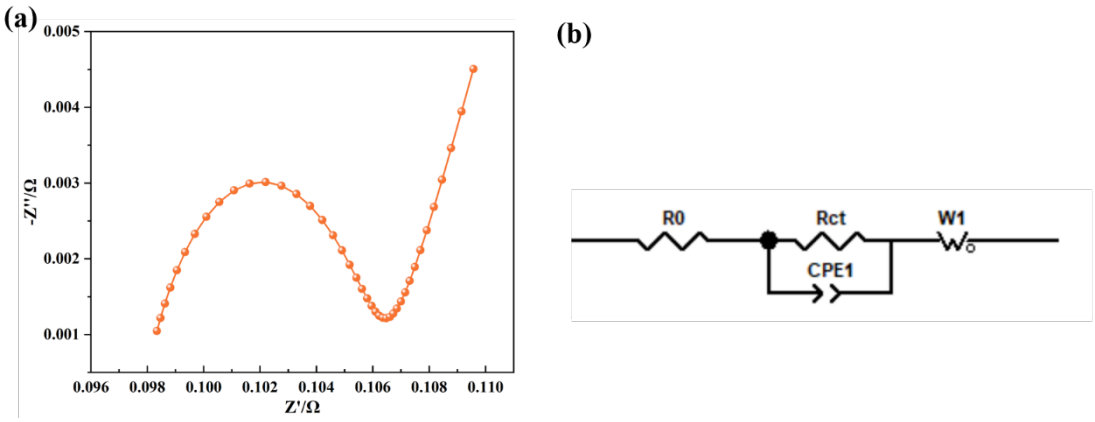

Figure 2: (a) Nyquist plot of EIS; (b) corresponding first-order RQ equivalent circuit model

2.3 DRT Analysis

In electrochemical systems, different electrochemical processes correspond to distinct relaxation time distributions, and thus, by extracting DRT, different electrochemical processes can be identified and understood (Shi et al., 2019). The DRT technique is implemented by fitting electrochemical impedance spectroscopy data to a general equivalent circuit model, which consists of an ohmic resistance in series with a set of parallel RC circuits composed of differential resistors and capacitor elements, as shown in Figure 3 (Leonide et al., 2009). The fundamental assumption of the DRT method is that the equivalent circuit of the electrochemical impedance spectrum of lithium-ion batteries consists of an ohmic resistance Ro in series with n RC circuits. The impedance spectrum can be expressed as an integral equation, as shown in Equation (1):

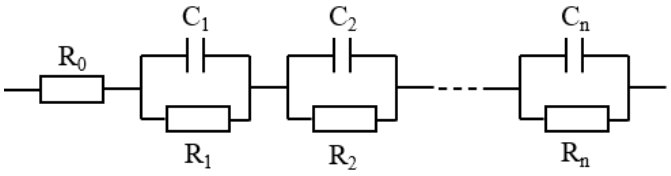

Figure 3: Equivalent circuit model based on distribution of relaxation

$$Z(\omega) = R_o + \int_0^{\infty} \frac{g(\tau)}{1 + j\omega\tau} \quad (1)$$

where, $Z(\omega)$ is the total impedance of the battery, Ro is the ohmic impedance of the system, τ is the relaxation time, $\frac{g(\tau)}{1+j\omega\tau}$ representing the polarization impedance in the τ to τ+dτ interval, and g(τ) is the function representing the system's time relaxation, indicating the infinite sum correlation of parallel R-C elements at each point in the time domain. The peaks of the function can be mapped to a discrete RC network, as proposed in an appropriate ECM (Wan et al., 2015).

Figure 4(a) presents the Nyquist plot of the electrochemical impedance spectroscopy (EIS) data, while Figure 4(b) shows the corresponding DRT described by the distribution function $\gamma(\tau)$. After deconvolution using the DRT analysis, the EIS data can be resolved into five characteristic peaks, labeled P1, P2, P3, P4, and P5 in order of increasing relaxation time. The peak area of each characteristic peak corresponds to the polarization resistance of the associated polarization process, while the relaxation time distribution of the peak reflects the rate of the polarization process. A comparison of Figure 2(b) and Figure 4(b) demonstrates that the DRT effectively deconvolutes coupled kinetic processes, thereby providing a powerful technical approach for investigating the aging mechanisms of lithium-ion batteries during cycling-induced degradation.

Although the DRT method offers advantages such as intuitive representation, high resolution, and the elimination of the need for equivalent circuit modeling, its numerical solution presents significant challenges. Due to the limited number of effective data points provided by EIS, combined with the DRT function being defined over a continuous interval (0, +∞), the process of inferring a large number of unknowns from sparse known information is mathematically ill-posed. Consequently, conventional numerical integration methods often fail to yield stable solutions (Rampf et al., 2025). Regularization techniques represent the predominant approach for computing the DRT function in current literature. Ciucci and coworkers introduced an innovative regularization method leveraging a radial basis function (RBF)-based pseudospectral algorithm for DRT deconvolution of EIS data, accompanied by the development of the DRTtools software for user-friendly visualization and operation (Delikaya et al., 2020). By optimizing parameters such as basis functions, data preprocessing, and regularization strength, this method significantly enhances the precision of DRT analysis (Kunaver et al., 2022). The key to solving the DRT function using regularization methods lies in selecting an appropriate regularization parameter λ, which controls the strength of regularization (Wang et al., 2025; Mama et al., 2025). In this study, the regularization parameter λ for DRT analysis was set to 1×10^{-3}. The DRT-processed EIS data yield spectra containing characteristic peaks at different relaxation times, with the number of peaks corresponding to the number of polarization processes in the electrochemical system.

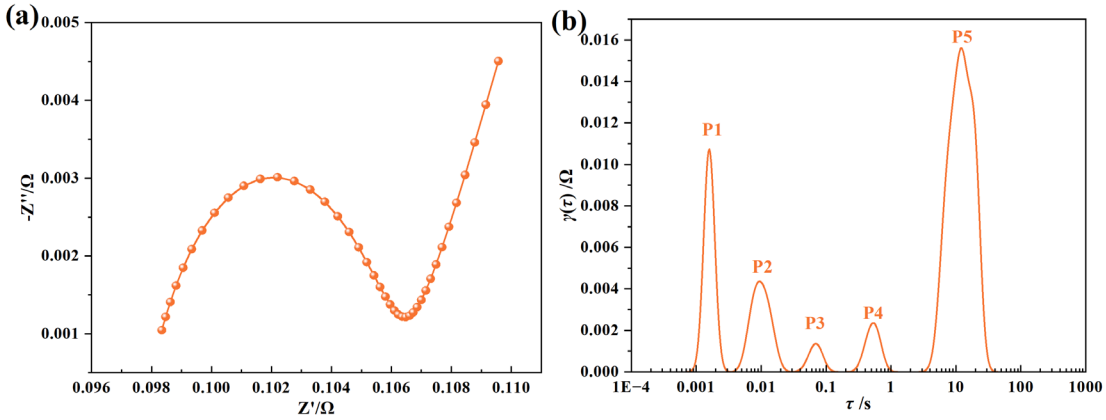

Figure 4: (a) Nyquist plot of EIS; (b) DRT plot described by the distribution function $\gamma(\tau)$

3. Results and Discussion

3.1 EIS Data Analysis

Figure 5(a), (b), (c), (d), (e), and (f) depict the EIS spectra of the Gra||NCM523 battery at different cycle numbers (CN20, CN40, CN80, CN100, CN160, CN240), with controlled charge voltages of 3.2 V → 3.4 V → 3.6 V → 3.8 V → 4.0 V → 4.2 V, followed by controlled discharge voltages of 4.0 V → 3.8 V → 3.6 V → 3.2 V → 3.0 V. The tests were conducted at a temperature of 25°C, with a charge-discharge current of 1C and a voltage range of 3.0–4.2 V.

Figure 5 presents the EIS spectra of the Gra||NCM523 battery at cycle numbers CN20, CN40, CN80, CN100, CN160, and CN240, with controlled voltages during the charge and discharge processes set at 3.0 V, 3.2 V, 3.4 V, 3.6 V, 3.8 V, 4.0 V, and 4.2 V. The tests were conducted at a temperature of 25°C, with a charge-discharge rate of 1C and a voltage range of 3.0–4.2 V.

As observed from Figure 5, for the Gra||NCM523 lithium-ion battery, the EIS spectra under different cycle aging numbers and charge-discharge voltages exhibit highly similar shapes, each consisting of a semicircle in the mid-frequency region and a sloped line in the low-frequency region. Within the same cycle number, the ohmic resistance (R_{ohm}) shows fluctuating variations with different charge-discharge voltages, while the charge transfer resistance (R_{ct}) is closely correlated with the battery's state of charge (SOC) and exhibits significant changes.

Figure 6(a) shows the fitted values of the ohmic resistance (R_{ohm}) for the Gra||NCM523 battery at cycle numbers CN20, CN40, CN80, CN100, CN160, and CN240 under different charge-discharge voltages, and Figure 6(b) illustrates the variations in the fitted values of the charge transfer resistance (R_{ct}).

Figure 6(a) illustrates the overall variation of the ohmic resistance (R_{ohm}) and Figure 6(b) shows the charge transfer resistance (R_{ct}) as a function of cycle number for the lithium-ion battery, obtained through fitting with Zview software under different charge-discharge voltages during the investigated cycling process. From the figure, it is evident that within the same cycle number, the ohmic resistance (R_{ohm}) exhibits fluctuating variations under different charge-discharge voltages, showing no significant correlation with the battery's state SOC. As cycle aging progresses, R_{ohm} gradually increases. At cycle numbers 20, 40, 80, 100, 160, and 240, the average values of the ohmic resistance (R_{ohm}) are approximately 0.0424 Ω, 0.0455 Ω, 0.0600 Ω, 0.0600 Ω, 0.109 Ω, and 0.151 Ω, respectively. This indicates that the R_{ohm} value increases by approximately 2.6 times from CN20 to CN240, reflecting the progressive aging of the battery. In contrast, the charge transfer resistance (R_{ct}) exhibits a distinct variation pattern. Within the same cycle number, R_{ct} shows significant changes with varying charge-discharge voltages, displaying a *W*-shaped variation. However, as cycle aging progresses, the overall change in R_{ct} is not pronounced. The fitting results of the EIS equivalent circuit model reveal that the variation patterns of the ohmic resistance (R_{ohm}) and charge transfer resistance (R_{ct}) in nickel-cobalt-manganese (NCM) lithium-ion batteries during cycle aging are markedly different.

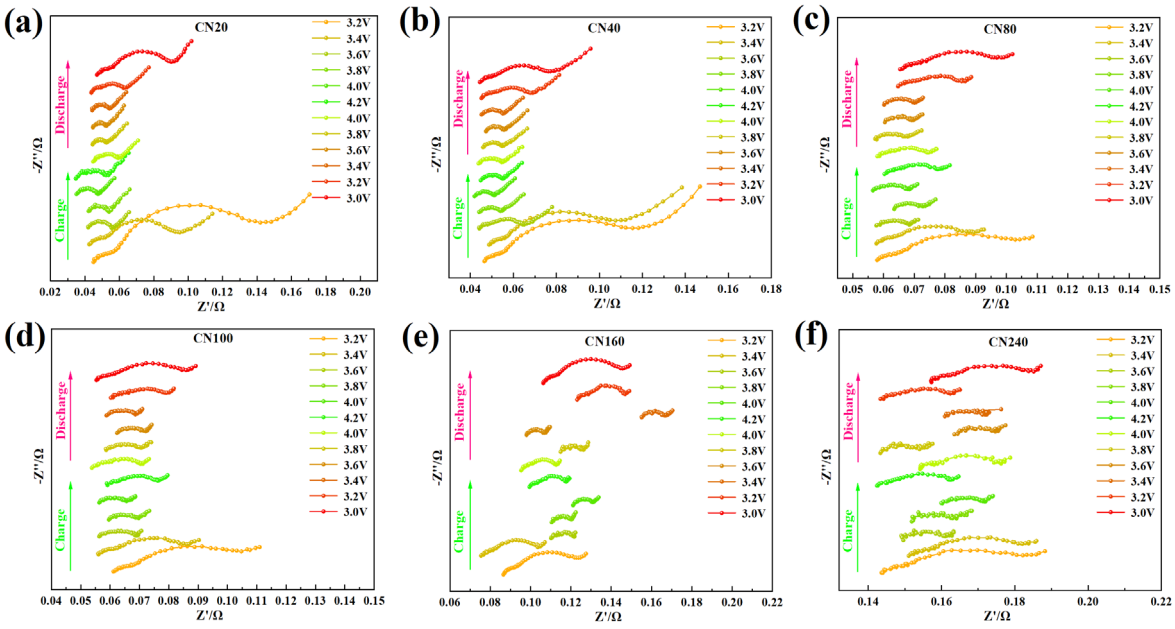

Figure 5: The Nyquist plots of the Gra||NCM523 battery in different cycle numbers and different voltages

Cite The Article: Wei, W. Q., Zhao, Y. M., He, Z. H., Du, Q. M., Wu, X. L., Chen, S. R., (2025). Aging Mechanism Analysis in Nickel-Cobalt-Manganese Ternary Batteries based on Drt Technology. *Advances in Industrial Engineering and Management, 14(1): 15-22. Doi: 10.7508/aiem.01.2025.15.22*

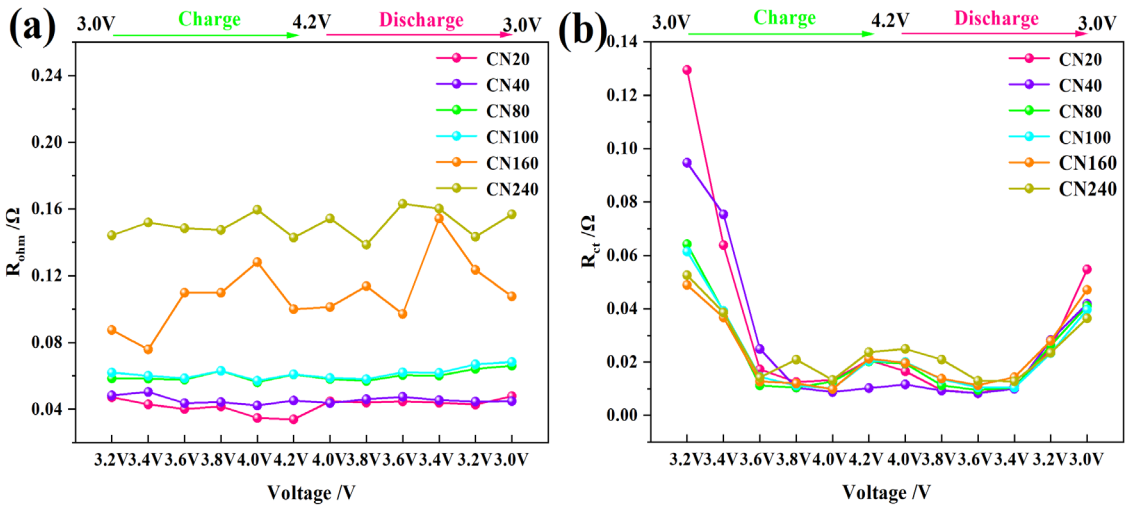

Figure 6: The change of (a) R_{ohm} and (b) R_{ct} in different cycle numbers and different voltages

3.2 Analysis of Drt Results

Figure 7(a), (b), (c), (d), (e), and (f) depict the time-dependent DRT evolution curves described by the distribution function $\gamma(\tau)$ for the Gra||NCM523 lithium-ion battery at different cycle numbers (CN20, CN40, CN80, CN100, CN160, CN240), with controlled charge voltages of 3.2 V → 3.4 V → 3.6 V → 3.8 V → 4.0 V → 4.2 V, followed by controlled discharge voltages of 4.0 V → 3.8 V → 3.6 V → 3.2 V → 3.0 V. The tests were conducted at a temperature of 25°C, with a charge-discharge current of 1C and a voltage range of 3.0 – 4.2 V.

Figure 7 depicts the time-dependent DRT evolution curves described by the distribution function $\gamma(\tau)$ for the Gra||NCM523 battery at cycle numbers CN20, CN40, CN80, CN100, CN160, and CN240, with controlled voltages during the charge and discharge processes set at 3.0 V, 3.2 V, 3.4 V, 3.6 V, 3.8 V, 4.0 V, and 4.2 V. The tests were conducted at a temperature of 25°C, with a charge-discharge rate of 1C and a voltage range of 3.0–4.2 V.

As shown in Figure 7, under different cycle numbers and charge-discharge voltages, up to five DRT characteristic peaks, labeled P1, P2, P3, P4, and P5, are resolved. Based on the time scale analysis, these peaks are assigned in order of increasing relaxation time distribution to the formation of the solid electrolyte interphase (SEI) film, the formation of the cathode electrolyte interphase (CEI) film, the charge transfer process at the anode, the charge transfer process at the cathode, and the solid-phase diffusion process, respectively (Lu et al., 2022). The occurrence of five characteristic peaks is primarily observed under conditions of low and high SOC for the battery. Throughout the majority of the lifecycle and across most charge-discharge voltages, the EIS data are resolved into only four DRT characteristic peaks, namely P1, P3, P4, and P5, with P2 being coupled into P3. In rare cases, the EIS data are resolved into only three DRT characteristic peaks, with both the P2 and P3 peaks being coupled into P4. This occurs, for example, at CN80 with a charge voltage of 3.2 V and at CN100 with a charge voltage of 3.2 V. With the progression of cycle aging and changes in the SOC, the DRT characteristic peaks exhibit distinctly different variation patterns. Peaks P3 and P5 increase or significantly increase at both extremely low and relatively high SOC conditions. In contrast, P1 shows fluctuating variations with different SOC levels, indicating no strong correlation with the battery's state of charge.

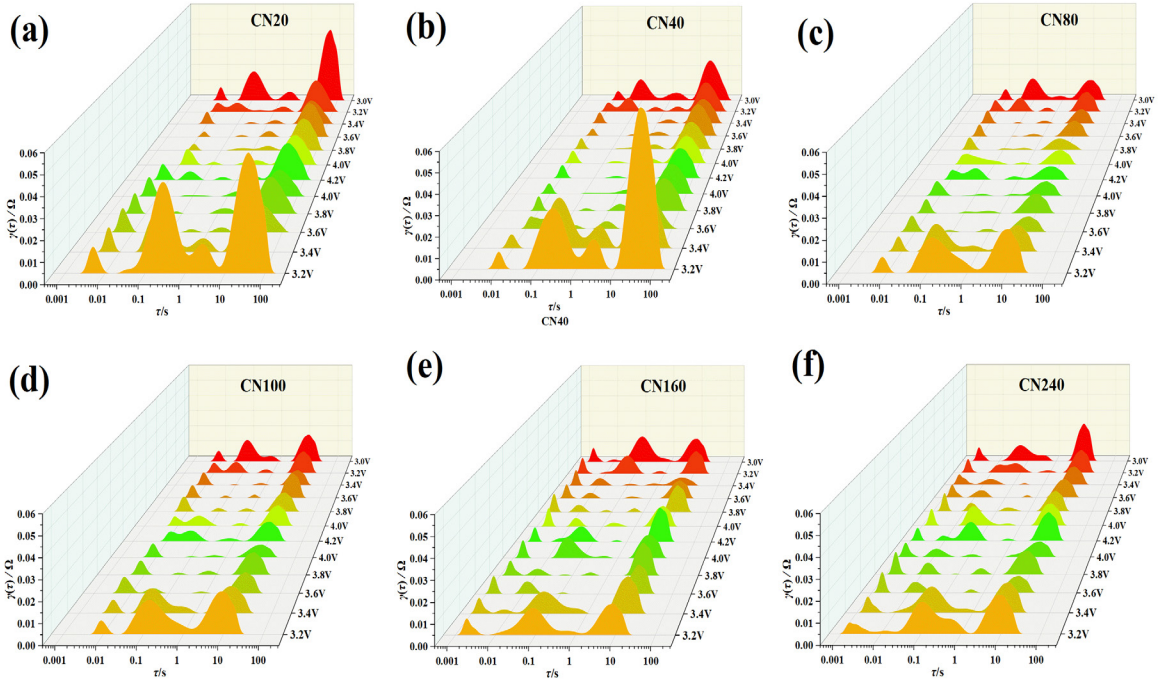

Figure 7: The temporal DRT evolution profiles of charging and discharging as described by the distribution function γ(τ) in different cycle numbers and different voltages

Figure 8 illustrates the variation curves of polarization resistance and time constants for the five characteristic peaks (P1, P2, P3, P4, P5) corresponding to different kinetic processes in the DRT analysis results for the Gra‖NCM523 battery at cycle numbers CN20, CN40, CN80, CN100, CN160, and CN240, with controlled voltages during the charge and discharge processes set at 3.0 V, 3.2 V, 3.4 V, 3.6 V, 3.8 V, 4.0 V, and 4.2 V. The tests were conducted at a temperature of 25 °C, with a charge-discharge rate of 1C and a voltage range of 3.0–4.2 V.

Figure 8(a), (b), (c), (d), (e), (f), (g), (h), (i), and (j) illustrate the variation curves of polarization resistance and relaxation time for the five kinetic processes (P1, P2, P3, P4, P5) derived from the DRT analysis results for the Gra‖NCM523 lithium-ion battery at different cycle numbers (CN20, CN40, CN80, CN100, CN160, CN240), with controlled charge voltages of 3.2 V → 3.4 V → 3.6 V → 3.8 V → 4.0 V → 4.2 V, followed by controlled discharge voltages of 4.0 V → 3.8 V → 3.6 V → 3.2 V → 3.0 V. The tests were conducted at a temperature of 25 °C, with a charge-discharge rate of 1C and a voltage range of 3.0–4.2 V.

For P1 (corresponding to the SEI film), as shown in Figure 8(a) and Figure 8(f), its impedance values (maximum 8.1×10^{-5} Ω, minimum 4.9×10^{-6} Ω, average 3.3×10^{-5} Ω) and relaxation times (maximum

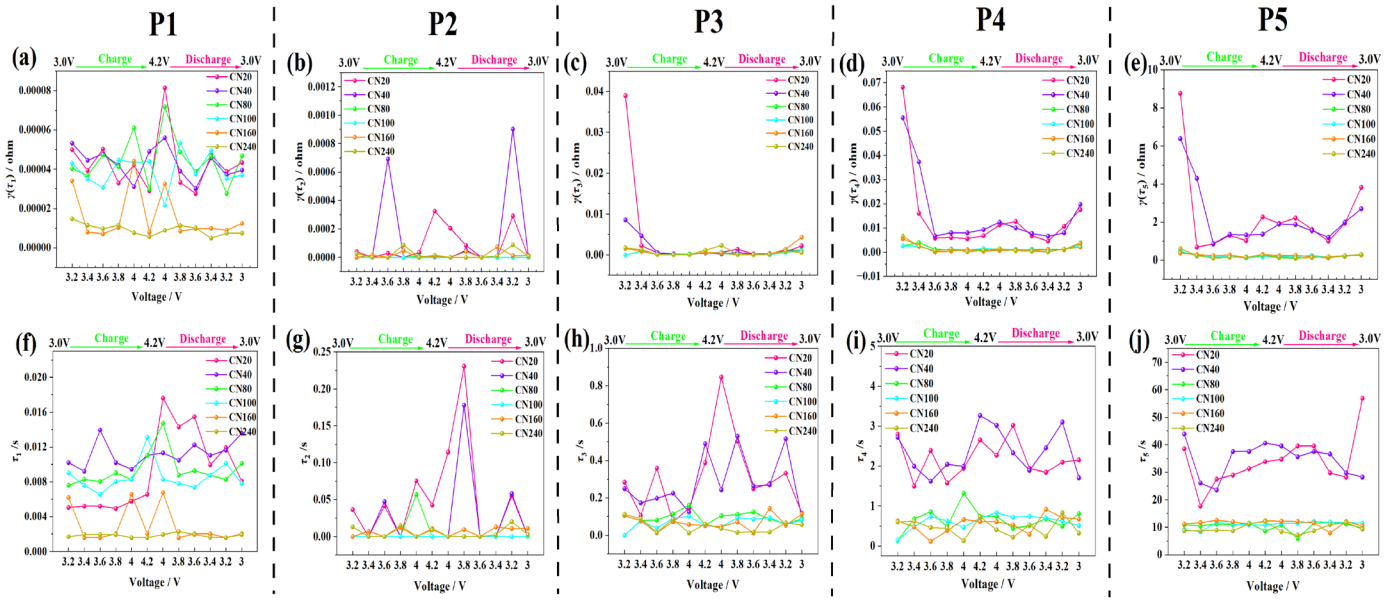

Figure 8: The evolution profiles of γ(τ) and τ in different cycle numbers and different voltages

Table 1: Quantitative Analysis Results of DRT

Cycle number	Statistical value	P1 (SEI layer)		P2 (CEI layer)		P3 (Li⁺ charge transfer anode/ electrolyte)		P4 (Li⁺ charge transfer cathode/ electrolyte)		P5 (Solid-state diffusion in electrodes)	
		$\gamma(\tau_1)\times10^{-5}$ /Ω	$\tau_1\times10^{-3}$ /s	$\gamma(\tau_2)\times10^{-5}$ /Ω	$\tau_2\times10^{-2}$ /s	$\gamma(\tau_3)\times10^{-4}$/Ω	$\tau_3\times10^{-2}$ /s	$\gamma(\tau_4)\times10^{-3}$ /Ω	τ_4 /s	$\gamma(\tau_5)$ /Ω	τ_5 /s
CN20	Max.	8.14	17.62	32.50	23.08	390.20	84.60	68.24	3.02	8.87	56.92
	Min.	2.76	4.93	/	/	0.53	7.17	4.58	1.50	0.68	17.68
	Ave.	4.29	9.17	8.39	4.97	39.87	30.65	14.34	2.18	2.29	33.89
CN40	Max.	5.60	13.95	90.27	17.80	85.80	53.00	55.60	3.27	6.38	43.90
	Min.	3.02	9.18	/	/	0.40	9.06	6.63	1.62	0.86	23.53
	Ave.	4.29	11.20	13.70	2.36	15.11	28.10	15.78	2.35	2.23	34.72
CN80	Max.	7.17	14.73	0.79	5.71	10.90	16.12	3.92	1.32	0.43	11.82
	Min.	2.76	7.59	/	/	/	/	0.79	0.14	0.097	5.92
	Ave.	4.48	9.35	0.066	0.48	3.60	8.86	1.64	0.66	0.20	10.37
CN100	Max.	5.35	13.13	/	/	9.92	10.16	2.76	0.83	0.48	12.17
	Min.	2.16	6.57	/	/	/	/	0.53	0.14	0.12	8.36
	Ave.	3.96	8.57	/	/	3.51	6.78	1.44	0.61	0.22	11.04
CN160	Max.	4.42	6.76	7.38	1.29	43.20	14.30	5.58	0.92	0.37	12.49
	Min.	0.71	1.59	/	/	0.26	1.21	0.049	0.12	0.12	7.96
	Ave.	1.61	3.00	1.75	0.62	8.15	6.79	1.49	0.55	0.24	11.42
CN240	Max.	1.48	2.29	8.89	2.02	23.21	11.29	6.64	0.84	0.61	12.08
	Min.	0.49	1.59	/	/	0.17	1.23	0.13	0.13	0.11	7.13
	Ave.	0.93	1.84	2.04	0.52	7.07	4.85	1.46	0.46	0.22	9.55

0.01762 s, minimum 1.6×10^{-3} s, average 7.2×10^{-3} s) gradually decrease with cycling and eventually stabilize. Specifically, at cycle numbers CN20, CN40, CN80, CN100, CN160, and CN240, the average impedance values for P1 are 4.3×10^{-5} Ω, 4.3×10^{-5} Ω, 4.5×10^{-5} Ω, 4.0×10^{-5} Ω, 1.6×10^{-5} Ω, and 9.3×10^{-6} Ω, respectively, and the average relaxation times are 9.2×10^{-3} s, 1.1×10^{-2} s, 9.4×10^{-3} s, 8.6×10^{-3} s, 3.0×10^{-3} s, and 1.8×10^{-3} s, respectively. From CN20 to CN240, the average impedance value decreases by 78.4%. Within the same cycle number, both impedance and relaxation time exhibit fluctuating variations under different SOC.

P2 (corresponding to the CEI film) is coupled in most cases, as clearly shown in Figure 7, and is only resolved under a few extreme conditions, such as specific cycle periods when the battery is in a low state of charge or high state of charge. The resolved P2 has an average impedance value of approximately 4.3×10^{-5} Ω and an average relaxation time of approximately 1.5×10^{-2} s.One of the reasons for the overall abnormal fluctuations in the impedance and relaxation time corresponding to P2 is its varying degree of coupling with other dynamic processes, and it also exhibits complex coupling variations with P3.

For P3 (anode charge-transfer resistance), as shown in Figures 8e and 8h, its impedance values (maximum 3.9×10^{-2} Ω, minimum 1.7×10^{-5} Ω, average 1.3×10^{-3} Ω) and relaxation times (maximum 0.85 s, minimum 0.012 s, average 0.14 s) exhibit overall minimal variation with cycling. Specifically, at CN20, CN40, CN80, CN100, CN160, and CN240, the average impedance values were 4.0×10^{-3} Ω, 1.5×10^{-3} Ω, 3.6×10^{-4} Ω, 3.5×10^{-4} Ω, 8.2×10^{-4} Ω, and 7.1×10^{-4} Ω, respectively, and the average relaxation times were approximately 0.31 s, 0.28 s, 0.09 s, 0.07 s, 0.07 s, and 0.05 s, respectively. The average impedance value decreased by approximately 82.25% from CN20 to CN240.However, within the same cycle period, the impedance variation under different SOC is relatively significant and correlated with the battery's state of charge. For example, at CN20, the highest impedance value corresponding to P3 is approximately 0.03902 Ω, while the lowest impedance value is approximately 5.3×10^{-5} Ω, differing by approximately 740-fold. The relaxation time corresponding to P3 varies in the range of 0.0717 to 0.846 s during the initial cycling period (CN20–CN40) and in the range of 0.01204 to 0.1612 s during the subsequent cycling process (CN80–CN240).

For P4 (cathode charge-transfer resistance), as shown in Figures 8d and 8i, its impedance values (maximum 6.8×10^{-2} Ω, minimum 4.9×10^{-5} Ω, average 6.0×10^{-3} Ω) and relaxation times (maximum 3.27 s, minimum 0.12 s, average 1.13 s) are generally higher during the initial cycling period, stabilizing after CN80. Specifically, at CN20, CN40, CN80, CN100, CN160, and CN240, the average impedance values were approximately 1.4×10^{-2} Ω, 1.6×10^{-2} Ω, 1.6×10^{-3} Ω, 1.4×10^{-3} Ω, 1.5×10^{-3} Ω, and 1.5×10^{-3} Ω, respectively, and the average relaxation times were 14.34 s, 15.78 s, 1.64 s, 1.44 s, 1.49 s, and 1.46 s, respectively. Within the same cycle period, the variation pattern of impedance values corresponding to P4 is similar to that of P3, exhibiting the highest impedance value at a low state of charge and a relatively high impedance value at a high state of charge, showing a *W*-shaped variation within the same cycle, with the pattern being more pronounce. The relaxation time of P4 exhibits fluctuating variations with different SOC. Specifically, during the initial cycling period (CN20–CN40), the relaxation time varies in the range of 1.498 to 3.267 s. As cyclic aging progresses, the relaxation time gradually decreases and stabilizes (0.116 to 1.322 s). Notably, the average impedance value at CN240, compared to CN20, decreased by 89.3%.

For P5 (solid-phase diffusion impedance), as shown in Figures 8e and 8j, its impedance values (maximum 8.77 Ω, minimum 0.097 Ω, average 0.9 Ω) and relaxation times (maximum 56.92 s, minimum 5.92 s, average 18.50 s) are generally higher during the initial cycling period, stabilizing after CN80, with a variation pattern very similar to that of P4. Specifically, at CN20, CN40, CN80, CN100, CN160, and CN240, the average impedance values were 2.29 Ω, 2.23 Ω, 0.20 Ω, 0.22 Ω, 0.24 Ω, and 0.22 Ω, respectively, and the average relaxation times were 33.89 s, 34.72 s, 10.37 s, 11.04 s, 11.42 s, and 9.55 s, respectively. Within the same cycle period, the variation pattern of impedance values corresponding to P5 is nearly synchronized with that of P4, exhibiting the highest impedance value at a low state of charge and a relatively high impedance value at a high state of charge, showing a pronounced *W*-shaped variation within the same cycle. The relaxation time corresponding to P5 also approximately exhibits a *W*-shaped variation with different SOC within the same cycle period.

For 18650 cylindrical batteries with NCM523 as the cathode material and graphite as the anode, during the cyclic aging process, five characteristic peaks, P1, P2, P3, P4, and P5, were resolved through DRT analysis, corresponding to five distinct dynamic processes: SEI film formation, CEI film formation, anode charge-transfer process, cathode charge-transfer process, and solid-phase diffusion process, respectively. The impedance values and relaxation times of P1, P2, P3, P4, and P5 are mutually coupled, but in the vast majority of cases, there are differences in orders of magnitude, enabling their separation and identification. The quantitative DRT analysis results indicate that the battery overall exhibits typical diffusion control (dominated by P5 variations). The variation pattern of the overall polarization processes resolved by DRT corresponds to and is consistent with the variation pattern of the polarization resistance R_{ct} obtained from equivalent circuit fitting in the first-order RQ model shown in Figure 6(b). Comparative analysis indicates that battery aging (characterized by a continuous increase in ohmic impedance during cycling) is not directly related to the evolution of all electrochemical polarization processes within the battery.

4. Conclusion

Addressing the high complexity of the dynamic processes and aging mechanisms in lithium-ion batteries, this study utilized 18650-type cylindrical lithium-ion batteries with nickel-cobalt-manganese ternary material $LiNi_{0.5}Co_{0.2}Mn_{0.3}O_2$ (NCM523) as the cathode and graphite as the anode (Gra‖NCM523), collecting EIS data at different cycle periods (CN20, CN40, CN80, CN100, CN160, CN240) and SOC(controlled charge-discharge voltages of 3.0 V, 3.2 V, 3.4 V, 3.6 V, 3.8 V, 4.0 V, 4.2 V). By integrating distribution of relaxation times (DRT) technology with equivalent circuit models, five distinct dynamic processes within the lithium-ion battery were successfully separated and quantitatively analyzed, leading to the following main conclusions:

(1) The EIS data were fitted using a first-order RQ equivalent circuit model to quantitatively analyze the overall variation trends of ohmic resistance R_{ohm} and charge-transfer resistance R_{ct} during the cycling process. During battery cyclic aging, the ohmic resistance R_{ohm} increased significantly with the number of cycles (a 2.6-fold increase from CN20 to CN240) and showed little correlation with the state of charge. In contrast, the charge-transfer resistance R_{ct} exhibited a *W*-shaped variation within the same cycle period, demonstrating a high dependence on the state of charge, but its overall aging trend was not significant, revealing distinct variation mechanisms between R_{ohm} and R_{ct}.

(2) Utilizing DRT technology to analyze EIS data, five dynamic processes within the battery were successfully separated, including SEI film formation, CEI film formation, anode charge-transfer process, cathode charge-transfer process, and solid-phase diffusion process. Quantitative analysis results indicate that, as cycling progresses, the battery's ohmic impedance continuously increases, whereas the electrochemical polarization impedance initially decreases significantly (corresponding to the battery's activation process) and subsequently stabilizes at 10–20% of the initial impedance. This suggests that battery aging (characterized by a continuous increase in ohmic impedance during cycling) is not directly related to the evolution of the main electrochemical polarization processes within the battery. The battery polarization exhibits typical diffusion control (dominated by P5 variations). The anode charge-transfer impedance, cathode charge-transfer impedance, and solid-phase diffusion impedance are highly dependent on the battery's SOC. Within the same cycle period, the impedance variations of the anode charge-transfer process P3, cathode charge-transfer process P4, and solid-phase diffusion process P5 can reach up to 740-fold. This study provides theoretical insights and data support for enhancing battery performance and mitigating internal polarization impedance.

Acknowledgments

This work is financially supported by the National Natural Science Foundation of China (No. 51973246) and by Natural Science Foundation of Henan province (242300420208, 252300420269).

References

Azizighalehsari, S., Boj, E. A., Venugopal, P., et al. (2024). A Distribution of Relaxation Time Approach on Equivalent Circuit Model Parameterization to Analyse Li-ion Battery Degradation. IEEE Transactions on Industry Applications.

Delikaya, Ö., Bevilacqua, N., Eifert, L., et al. (2020). Porous electrospun carbon nanofibers network as an integrated electrode@ gas diffusion layer for high temperature polymer electrolyte membrane fuel cells. Electrochimica Acta, 345, 136192.

He, R., He, Y., Xie, W., et al. (2023). Comparative analysis for commercial li-ion batteries degradation using the distribution of relaxation time method based on electrochemical impedance spectroscopy. Energy, 263, 125972.

Hu, W., Peng, Y., Wei, Y., et al. (2023). Application of electrochemical impedance spectroscopy to degradation and aging research of lithium-ion batteries. The Journal of Physical Chemistry C, 127(9), 4465-4495.

Iurilli, P., Brivio, C., Carrillo, R. E., et al. (2021). EIS2MOD: A DRT-based modeling framework for li-ion cells. IEEE Transactions on Industry Applications, 58(2), 1429-1439.

Iurilli, P., Brivio, C., Wood, V. (2022). Detection of Lithium-Ion Cells' Degradation through Deconvolution of Electrochemical Impedance Spectroscopy with Distribution of Relaxation Time. Energy Technology, 10(10), 2200547.

Jung, M. J., Lee, S. G., Choi, K. S. (2024). A new diagnostic indicator for lithium-ion batteries via electrochemical impedance spectroscopy: Harnessing the highest frequency peak in distribution of relaxation times. Journal of Power Sources, 611, 234743.

Kebede, M. A. (2023). Ni-rich LiNixCoyM1-x-yO2 (NCM; M= Mn, Al) cathode materials for lithium-ion batteries: Challenges, mitigation strategies, and perspectives. Current Opinion in Electrochemistry, 39, 101261.

Kharal, A. Y., Khalid, M., Naqvi, I. H., et al. (2025). Identification and quantification of degradation modes in lithium-ion battery cells under dynamic load conditions using equivalent circuit and physics-based models. Journal of Power Sources, 632, 236274.

Kunaver, M., Rojec, Ž., Subotić, V., et al. (2022). Extraction of distribution function of relaxation times by using drt-rblm tools: A new approach to combine levenberg-marquardt algorithm and radial basis functions for discretization basis. Journal of The Electrochemical Society, 169(11), 110529.

Leonide, A., Apel, Y., Ivers-Tiffee, E. (2009). SOFC modeling and parameter identification by means of impedance spectroscopy. ECS Transactions, 19(20), 81.

Lu, Y., Zhao, C. Z., Huang, J. Q., et al. (2022). The timescale identification decoupling complicated kinetic processes in lithium batteries. Joule, 6(6), 1172-1198.

Mama, M., Solai, E., Capurso, T., et al. (2025). Comprehensive review of multi-scale Lithium-ion batteries modeling: From electro-chemical dynamics up to heat transfer in battery thermal management system. Energy Conversion and Management, 325, 119223.

Maradesa, A., Py, B., Ciucci, F. (2024b). Probabilistic deconvolution of the distribution of relaxation times from multiple electrochemical impedance spectra. Journal of Power Sources, 621, 235236.

Maradesa, A., Py, B., Huang, J., et al. (2024a). Advancing electrochemical impedance analysis through innovations in the distribution of relaxation times method. Joule.

Patel, B., Sorrentino, A., Vidakovic-Koch, T. (2025). Data-driven analysis of electrochemical impedance spectroscopy using the Loewner framework. iScience, 28(3).

Plank, C., Rüther, T., Jahn, L., et al. (2024). A review on the distribution of relaxation times analysis: A powerful tool for process identification of electrochemical systems. Journal of Power Sources, 594, 233845.

Rampf, A., Marchfelder, C., Zeis, R. (2025). Distribution of relaxation times analysis of rotating disk electrode impedance spectra. Electrochimica Acta, 514, 145583.

Rüther T, Schamel M, Plank C, et al. (2023). Cell-to-cell variation beyond parameter analysis—Identification and correlation of processes in Lithium-Ion Batteries using a combined distribution of relaxation times analysis. Journal of Power Sources, 587, 233677.

Sadeghi, E., Gholami, M. M., Hamzeh, M., et al. (2023). A systematic overview of power electronics interfaced electrochemical impedance spectroscopy for energy storage systems. Journal of Energy Storage, 62, 106850.

Shi, W., Jia, C., Zhang, Y., et al. (2019). Differentiation and decomposition of solid oxide fuel cell electrochemical impedance spectra. Acta Physico-Chimica Sinica, 35, 509-516.

Siroma, Z., Kuratani, K. (2025). New method for graphing impedance values as an analytical tool suitable for electrochemical impedance spectroscopy. Electrochimica Acta, 509, 145305.

Sohaib, M., Akram, A. S., Choi, W. (2025). Identifying Failure Conditions in Li-Ion Batteries Using Distribution of Relaxation Time Method. Authorea Preprints.

Wan, T. H., Saccoccio, M., Chen, C., et al. (2015). Influence of the discretization methods on the distribution of relaxation times deconvolution: implementing radial basis functions with DRTtools. Electrochimica Acta, 184, 483-499.

Wang, Y., Xiang, H., Soo, Y. Y., et al. (2025). Aging mechanisms, prognostics and management for lithium-ion batteries: Recent advances. Renewable and Sustainable Energy Reviews, 207, 114915.

Zhang, W., Ahmed, R., Habibi, S. (2025). Understanding the impact of recent usage on lithium-ion battery impedance through the relaxation phenomena. Journal of Power Sources, 630, 236108.

Zhou, X., Huang, J., Pan, Z., et al. (2019). Impedance characterization of lithium-ion batteries aging under high-temperature cycling: Importance of electrolyte-phase diffusion. Journal of Power Sources, 426, 216-222.

Cite The Article: Wei, W. Q., Zhao, Y. M., He, Z. H., Du, Q. M., Wu, X. L., Chen, S. R., (2025). Aging Mechanism Analysis in Nickel-Cobalt-Manganese Ternary Batteries based on Drt Technology. *Advances in Industrial Engineering and Management, 14(1): 15-22. Doi: 10.7508/aiem.01.2025.15.22*